Membrane Tension, Lipid Adaptation, Conformational Changes, and Energetics in MscL Gating

Huan Rui, Ritesh Kumar, and Wonpil Im*
Department of Molecular Biosciences and Center for Bioinformatics, The University of Kansas, Lawrence, Kansas

ABSTRACT   This study aims to explore gating mechanisms of mechanosensitive channels in terms of membrane tension, membrane adaptation, protein conformation, and energetics. The large conductance mechanosensitive channel from *Mycobacterium tuberculosis* (Tb-MscL) is used as a model system; Tb-MscL acts as a safety valve by releasing small osmolytes through the channel opening under extreme hypoosmotic conditions. Based on the assumption that the channel gating involves tilting of the transmembrane (TM) helices, we have performed free energy simulations of Tb-MscL as a function of TM helix tilt angle in a dimyristoylphosphatidylcholine bilayer. Based on the change in system dimensions, TM helix tilting is shown to be essentially equivalent to applying an excess surface tension to the membrane, causing channel expansion, lipid adaptation, and membrane thinning. Such equivalence is further corroborated by the observation that the free energy cost of Tb-MscL channel expansion is comparable to the work done by the excess surface tension. Tb-MscL TM helix tilting results in an expanded water-conducting channel of an outer dimension similar to the proposed fully open MscL structure. The free energy decomposition indicates a possible expansion mechanism in which tilting and expanding of TM2 facilitates the iris-like motion of TM1, producing an expanded Tb-MscL.

INTRODUCTION

Mechanosensation is an essential biological process by which cells respond to external environmental changes (1,2). Various forms of life from bacteria to mammals can detect external stimuli (e.g., pressure, touch, balance, and pain) via mechanosensitive (MS) channels and take corresponding actions. Among various MS channels with specific functions assigned, bacterial MS channels protect cells from lysis by releasing small osmolytes through the channel opening under extreme hypoosmotic conditions (3). Based on their conductance level in *Escherichia coli*, MS channels are classified into three families (4): MscM with mini conductance (~0.5 nS), MscS with small conductance (~1 nS), and MscL with large conductance (~3 nS). Among these families, MscL is the first cloned and the most studied MS channel (5).

The crystal structure of MscL homolog from *Mycobacterium tuberculosis* (Tb-MscL) reveals a homopentameric architecture with each monomer having N- and C-terminal domains at the cytoplasmic side and a two-helix transmembrane domain (TM1 and TM2) connected by a periplasmic loop (Fig. 1) (6). The structure represents a closed state with the TM1 helices lining the channel lumen and the TM2 helices in contact with the lipid bilayer. Five Val-21 residues form a constriction gate blocking the channel near its cytoplasmic opening. MscL gating is tension-dependent; there exist several intermediate conducting states when the channel undergoes closed to fully open transition (7). An expanded intermediate state was recently revealed by a crystal structure of MscL homolog from

Staphylococcus aureus (Sa-MscL) (8) with a periplasmic area of ~2200 Å^2, which is similar to that of a proposed fully open MscL (7), and a constriction zone of ~3 Å radius.

Considerable efforts have been made to elucidate the gating mechanisms of MscL. Patch clamp experiments show that Eco-MscL (from *E. coli*) is activated by an applied membrane tension of 8–12 dyn/cm, depending on the membrane environments (7,9). Using the same patch clamp experiment in conjunction with kinetic and thermodynamic analysis (7,10), a free energy difference of ~30.6 kcal/mol was estimated between the closed and fully open Eco-MscL in a membrane without applied tension. On the other hand, various computational methods, such as molecular dynamics (MD) simulations of MscL in a curved bilayer (11), steered MD simulations to stretch open the channel (12), and continuum elastic modeling of the channel (13,14), have been applied to investigate tension-induced MscL conformational changes. Despite these efforts, the following fundamental questions still need to be addressed to fully understand the tension-induced gating mechanism; i), how is the applied tension perceived by both the membrane and MscL? More specifically, what are the extents of hydrophobic match between MscL and the surrounding membrane and how much does the local membrane thickness deviate from that of the bulk membrane (i.e., the membrane adaptation) to accommodate such a hydrophobic match? ii), what are the structural changes of MscL upon tension increase, and iii), what is the free energy associated with such structural changes?

This work aims to elucidate the relationship between applied membrane tension and the channel conformation in atomic detail and provide insights into the energetics during the channel gating process. For a channel like
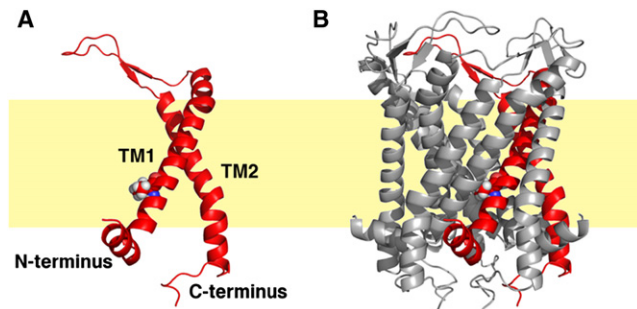
FIGURE 1   Molecular representation of MscL (*A*) monomer and (*B*) pentamer. Each monomer has two transmembrane helices, TM1 and TM2, and cytosol-facing N- and C-termini. The lipid bilayer is illustrated by the yellow slab. Also shown is the constriction zone residue Val-21 highlighted in sphere presentation. The figures are prepared using PyMOL (51).

MscL to achieve an open state with an estimated radius of 15–20 Å (7), TM helix rearrangements must take place. In particular, either the pore-facing TM helices have to increase their tilt angles or more TM helices have to be present to line the channel wall. Many experimental evidences favor the former. For example, the electron paramagnetic resonance experiments of Eco-MscL trapped in an open state showed little difference in solvent accessibility of TM2 residues between the closed and open state (15) and the modeling of open Eco-MscL with both TM1 and TM2 helices facing the channel pore leads to an open channel with smaller radius than the expected 15–20 Å and exposure of the hydrophobic residues to the lumen. Taking these evidences into consideration, we adopted the hypothesis that the MscL opening is achieved predominantly by TM helix tilting, and performed a total of 1.2-μs umbrella sampling free energy MD simulations of Tb-MscL in dimyristoylphosphatidylcholine (DMPC) bilayers at a series of TM tilt angles. The results are presented and discussed in terms of the relationship between TM helix tilting and applied surface tension, the impact of TM helix tilting on lipid properties, channel conformational changes, and the energetics. On the basis of these observations, possible mechanisms of Tb-MscL expansion and gating are discussed.

MATERIALS AND METHODS

Simulations of Tb-MscL in a DMPC bilayer

The Tb-MscL crystal structure (PDB:2OAR) (6) was used for all simulations. Assuming MscL gating is driven by tension-induced TM helix tilting, we have explored the possible gating mechanisms by applying the helix tilt restraint potential to the TM helices (TM1 and TM2) of Tb-MscL in a DMPC bilayer; the restraint potential holds TM tilt angles at their target values (16). Although other lipid bilayers like 1-palmitoyl-2-oleyl-*sn*-glycero-3-phosphoethanolamine, dioleoylphosphatidylcholine, and dioleoylphosphatidylglycerol could be used in molecular simulations, exploring impacts of different lipids on the MscL gating properties is beyond the scope of the current study. An initial system of Tb-MscL in DMPC bilayers bathed in 0.5 M KCl was generated using the Membrane Builder module

(17,18) in CHARMM-GUI (19). Although ~10% decrease in gating tension threshold and ~20% higher gating energy were observed for Eco-MscL after truncation of C-terminal residues (Ala-110-Ser-136) in one set of experiments (20), no significant change in gating tension sensitivity was found in an earlier study (21). Because the C-terminus truncated mutant can still reach the same fully open state as the wild-type channel (20,21), the C-terminal helix (Gln-110-Asn-125) in Tb-MscL was excised to reduce the number of atoms in the system.

To accommodate the expansion of the system size in the *XY* axes upon helix tilting, we used NPγT (constant pressure, surface tension, and temperature) dynamics (22) with a pressure of 1 atm along the *Z* direction (the membrane normal), a surface tension of 20 dyn/cm, and a temperature of 303.15 K. The 20 dyn/cm surface tension was applied to avoid the freezing of lipid tails in the CHARMM lipid force field (23,24), and it was shown that such surface tension values do not perturb the energetics (25); n.b., this work was initiated much earlier than the release of the new lipid force field (26), which allows NPT simulations without chain freezing. Because the system size along the *Z* axis (L_z) decreases as the system size expands along *XY*, the initial system was built to have a relatively large L_z (L_z = 110 Å). Considering possible asymmetric expansions in the cytoplasmic and periplasmic sides of Tb-MscL, we used P2$_1$ image transformation (27) to allow the variation in the number of lipids at the top and bottom leaflets during the simulation. The final system consisted of one Tb-MscL, 201 DMPC molecules, 177 K$^+$ ions, 182 Cl$^-$ ions, and 20,534 water molecules, resulting in a total of 94,174 atoms.

All calculations have been done using the biomolecular simulation program CHARMM (28) with the all-atom parameter set PARAM22 (29) including the dihedral cross-term corrections (CMAP) (30) and a modified TIP3P water model (31). We first equilibrated the initial systems with 450 ps NPAT (constant area) dynamics followed by 450 ps NPγT dynamics with the nonbonded and dynamics options in the Membrane Builder inputs; the van der Waals interactions were smoothly switched off at 11–12 Å by a force switching function (32) and the electrostatic interactions were calculated using the particle-mesh Ewald method with a mesh size of ~1 Å for fast Fourier transformation, $\kappa = 0.34$ Å^{-1}, and a sixth-order B-spline interpolation (33).

We defined the TM1 (Ile-14-Ile-38) and TM2 (Leu-69-Val-91) helices according to the original published literature (34). The tilt angle (τ) was defined as the angle between the helical axis and the membrane normal (*Z* axis). The helix tilt restraint potential (16) was then applied to both TM1 and TM2 to set up 30 simulation systems ($\delta\tau_1$ to $\delta\tau_{30}$). The systems were generated by tilting both TM helices simultaneously in 1° increment every 200 ps, i.e., gradually varying τ of TM helices together from 35° to 64° (TM1) and 33° to 62° (TM2), respectively. Because the tilt angle differences between the closed and modeled open states for TM1 and TM2 are similar (6,15), we decided to tilt the TM segments together. After generating the initial windows, we have performed a total of 40-ns umbrella sampling MD simulation for each system. Fig. S1, *A* and *B* in the Supporting Material show the final systems of $\delta\tau_1$ and $\delta\tau_{30}$.

Potential of mean force of TM helices tilting and its decomposition

The free energy profile of each TM helix, $G_{TM}(\tau)$, as a function of τ was calculated by the mean force integration method (35–37), i.e., by integrating the mean force, $\langle \mathbf{F}(\tau) \rangle_\tau$, along τ,

$$\frac{dG_{TM}(\tau)}{d\tau} = -\langle \mathbf{F}(\tau) \rangle_\tau = \left\langle \frac{\partial U(\mathbf{r})}{\partial \tau} - k_B T \frac{\partial \ln |J|}{\partial \tau} \right\rangle_\tau, \quad (1)$$

where k_B, $U(\mathbf{r})$, and $|J|$ are the Boltzmann constant, the system potential energy, and the Jacobian related to the transformation of the coordinate system, respectively (16). The potential of mean forces (PMFs) calculated using Eq. 1 is compatible with those calculated from the weighted

histogram analysis method (38) (data not shown). Based on the equivalence between the PMF and the thermodynamic reversible work along the reaction coordinate, the total PMF can be decomposed into contributions arising from various microscopic forces (35). In this study, the total PMF is decomposed into the physically relevant contributions from helix conformation and helix-helix interactions (G_{TM-TM}), helix-membrane interactions ($G_{TM-MEMB}$), and helix-solvent interactions ($G_{TM-SOLV}$). It should be noted that the helix conformation term in G_{TM-TM} includes two components: one from the helix conformational change (G_{conf}) and the other from the helix orientational change. The first term, G_{conf}, consists of the total self-energy of the TM helices and contributions from interactions between TM and the rest of the protein; the latter corresponds to the TM helix orientational entropy (G_{pre}) related to accessible precession space of the helix when it tilts and is represented by the Jacobian term in Eq. 1 (16). Because the G_{pre} contribution is very small for $\tau > 20°$, which is the case in this study, its contribution to the total PMF is not considered.

MscL cross-sectional area calculation

Both the solvent accessible area inside the pore (A_{pore}) and the in-plane area of the channel ($A_{in-plane}$) were calculated from the averaged structure of the last 30-ns simulation in each system. To define the solvent accessible area, the CHARMM PARAM22 Lennard-Jones radii were scaled by $2^{-1/6}$ (to obtain the contact radii) and then increased by a probe radius of 1.4 Å. A grid-based search with a 0.2 Å grid spacing was performed for slabs along the Z axis. The slabs were defined differently in A_{pore} and $A_{in-plane}$ calculations for the purpose of comparison with experimental measurements. In the case of A_{pore}, the Z length of every four residues along TM1 from Ile-14 to Thr-35 was chosen to define a slab. The A_{pore} for each slab was then calculated as the difference between the area of both the protein and solvent and the protein-only area. For $A_{in-plane}$, a slab length of 4.0 Å along the Z axis was used from -12.5 Å to 12.5 Å in 0.1 Å increments, and $A_{in-plane}$ was calculated by the total area of both the protein and solvent in a given slab.

RESULTS AND DISCUSSION

TM helix tilting and excess surface tension

Our simulation study is based on the hypothesis that TM helix tilting is the major initial response to the applied excess membrane tension during the tension-dependent closed-to-open transition, and TM helix tilting would result in the similar conformation change of the channel as the excess tension applied in experiments. To examine such correspondence between TM helix tilting ($\delta\tau$, simulation) and the applied excess tension (γ_{ex}, experiment), γ_{ex} was estimated for each $\delta\tau$ system based on the area compressibility (K_a) and the area change (ΔA) of the whole system due to TM helix tilting (39),

$$\gamma_{ex} = \frac{1}{2}K_a\frac{\Delta A}{A_0}, \qquad (2)$$

where A_0 is the area in system $\delta\tau_1$ and ΔA is the area deviation from A_0. K_a can be computed from the average area $\langle A \rangle$ and its fluctuation $\langle \delta A^2 \rangle$ in each $\delta\tau$ system,

$$K_a = k_B T \frac{\langle A \rangle}{\langle \delta A^2 \rangle}. \qquad (3)$$

Fig. S2 A shows that K_a is roughly similar for most systems with an average of 135 ± 46 dyn/cm, similar to the experimentally measured K_a in a pure DMPC bilayer (40). Considering the difference between the systems, γ_{ex} is evaluated independently for each system using the corresponding K_a value. It should be noted that there is no actual γ_{ex} explicitly applied to each system during the simulations, and γ_{ex} is the tension required to achieve similar system expansion in the XY plane (due to TM helix tilting). Therefore, γ_{ex} is different from the surface tension (γ) employed in the NPγT simulations, which is the same in all $\delta\tau$ systems (Fig. S2 B) and was applied to avoid freezing of lipid tails with the previous CHARMM lipid force field (see Materials and Methods).

Fig. 2 A shows a linear relationship between γ_{ex} and $\delta\tau$; γ_{ex} reaches up to 22.0 ± 10.7 dyn/cm at $\delta\tau = 30°$. Indeed, tilt angle increase in the TM helices corresponds to the increment in γ_{ex} that is necessary to achieve similar system expansion in the XY plane. Emphasis, though, should not be placed on the absolute values of the calculated γ_{ex} because of the following concerns. First, Tb-MscL requires twice larger
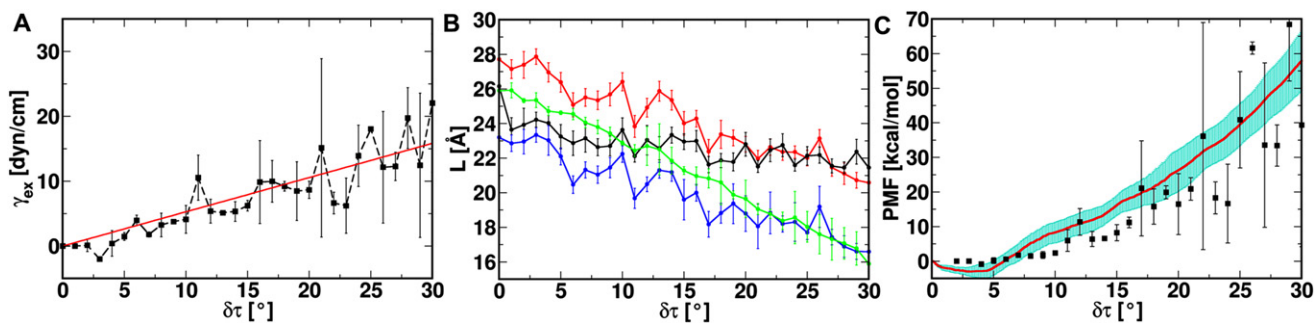

FIGURE 2 (*A*) Excess membrane tension (γ_{ex}) and its standard error as a function of $\delta\tau$ with its linear interpolation (*red*). (*B*) The thickness of the contact lipid bilayer ($L_{contact}^{C2}$ and $L_{contact}^{C22}$ in *red* and *blue*, respectively), the noncontact lipid bilayer ($L_{noncontact}^{C2}$ in *black*), and the hydrophobic length of TM2 along the Z axis (L^{TM2} in *green*). $L_{contact}^{C2}$ and $L_{noncontact}^{C2}$ are defined as the average distances between the C2 atoms, the second carbon in the glycerol moiety, in the top and bottom leaflets of the contact and noncontact lipids, respectively. $L_{contact}^{C22}$ is defined in the same fashion but with C22/C32 atoms, which are the first methylene carbons in the lipid acyl chains. L^{TM2} is defined by the span of backbone atoms on TM2 helices along the Z axis. (*C*) The total PMF (*red*) of Tb-MscL as a function of $\delta\tau$. Its SD (*cyan*) is calculated by sequentially dividing the last 30-ns trajectory in each $\delta\tau$ window into six pieces of 5-ns duration. Also shown is the work done by the excess tension ($\Delta G_{TENSION}$) in solid circles (*black*).

gating tension than Eco-MscL in the same membrane patch (41). Second, gating tension of MscL is sensitive to the hydrophobic thickness of the membrane (42) and the tension threshold of Eco-MscL gating was measured in *E. coli* membranes (7), which are predominantly composed of 1,2-dioleoyl-phosphatidylethanolamine with 18 carbon atoms on the lipid acyl chain. Last, the gating tension depends on the headgroup of the lipid in a membrane (9). Despite these differences that limit the comparison between the calculated γ_{ex} and the experimental values, water permeation is detected after $\delta\tau = 16°$ and an expanded channel is achieved. This expanded state of Tb-MscL does not conduct ions and is structurally different than the proposed fully opened channel (see below). To reach a fully open state, TM helix rearrangement may take place after the TM tilting, and the time scale of such an event is beyond the current simulations. Nevertheless, we can characterize membrane bilayer properties that converge quickly in simulations to explore the response of the bilayer and the protein-lipid interactions upon TM helix tilting. Because of the correspondence between $\delta\tau$ and γ_{ex}, the same response is expected when an actual surface tension is applied in experiments.

Influence of TM helix tilting on lipid bilayer properties

Bilayer thinning is observed during the course of Tb-MscL TM helix tilting (Fig. S1). Because the extent of bilayer thinning can be different depending on the proximity of the lipids to Tb-MscL, the thinning effects are examined separately for lipids that are in contact with or far away from the protein; a distance criterion of 4 Å from MscL heavy atoms is employed to distinguish the two types of lipids. As shown in Fig. 2 *B*, the thickness of the contact lipid bilayer ($L_{contact}^{C2}$) is more affected by the $\delta\tau$ increment than that of the noncontact bilayer ($L_{noncontact}^{C2}$); the thinning magnitudes are 7.1 ± 0.4 Å (contact) and 4.7 ± 0.4 Å (noncontact) at $\delta\tau = 30°$. This is because the local lipids are in direct contact with the channel, and are more sensitive to TM tilting. Based on the theory of elastic bilayer deformation, Ursell et al. (43) estimated that the bilayer deformation extends ~30 Å from the channel wall. As shown in Table S1, the present simulation dimension in *XY* is smaller to measure the bulk lipid properties, but the difference between $L_{contact}^{C2}$ and $L_{noncontact}^{C2}$ can readily illustrate the local bilayer deformation.

Interestingly, the membrane bilayer adaptation also changes in response to TM helix tilting; the adaptation is defined as $\Delta L = L_{contact}^{C2} - L_{noncontact}^{C2}$ with positive and negative values indicating local membrane thickening and thinning, respectively. ΔL is relatively large at small $\delta\tau$ (e.g., 3.4 ± 0.9 Å at $\delta\tau = 1°$), but it starts to vanish as $\delta\tau$ increases and becomes only $-0.8 ± 0.6$ Å at $\delta\tau = 30°$. The ΔL change as a function of $\delta\tau$ indicates the adjustment of the local lipid bilayer to maximize the hydrophobic match between TM2 of Tb-MscL and the lipid bilayer in the course

of TM helix tilting. Fig. 2 *B* also shows the effective hydrophobic length of TM2 along the *Z* axis (L^{TM2}) and the hydrophobic thickness of the contacting bilayer ($L_{contact}^{C22}$) measured between the first methylene carbons in the lipid tails of the top and bottom leaflets. Although the gap between L^{TM2} and $L_{contact}^{C2}$ grows along $\delta\tau$, L_{TM2} is always in between $L_{contact}^{C2}$ and $L_{contact}^{C22}$, implying that the lipid hydrophobic/hydrophilic transition region between the second carbon (C2) in the glycerol moiety and the first methylene carbons (C22/C32) in the lipid tails allows a freedom of TM2 positioning in the bilayer while still maintaining the maximal hydrophobic match. Such optimal hydrophobic interactions even at large $\delta\tau$ stabilizes the expanded MscL and facilitates the opening process.

Conformational changes of Tb-MscL upon TM helix tilting

The structural changes and stability of Tb-MscL during the umbrella sampling simulations are examined by the root mean-square deviation (RMSD), the root mean-square fluctuation, and the TM helicity (Fig. S3). Fig. S3 *A* shows the RMSD of the TM helix backbone from the crystal structure as a function of time for the $\delta\tau_1$, $\delta\tau_{10}$, $\delta\tau_{20}$, and $\delta\tau_{30}$ systems; the time averages of the RMSD are 1.2 ± 0.1, 3.0 ± 0.1, 5.3 ± 0.1, and 7.9 ± 0.3 Å, respectively. Clearly, TM helix tilting results in structural changes (channel opening, see below). However, the small RMSD fluctuation in each system, mostly <0.4 Å, indicates minimal conformational changes within each $\delta\tau$ system. The root mean-square fluctuation in Fig. S3 *B* shows similar trends in each system; as anticipated, the TM regions exhibit minor structural fluctuation, whereas much higher flexibility is observed for the residues in the terminal and loop regions. The TM helicity in Fig. S3 *C* illustrates the integrity of the TM helix structure during the simulations; both TM1 and TM2 maintain helicity above 80% even with large tilt angles. Based on the stability of Tb-MscL in all simulations, the following analyses are performed for the last 30-ns trajectories to investigate the conformational changes associated with the channel opening process.

TM helix tilting is accompanied by Tb-MscL channel expansion. Fig. 3 *A* plots the average channel pore area (A_{pore}) along TM1 residues in systems $\delta\tau_1$, $\delta\tau_{10}$, $\delta\tau_{20}$, and $\delta\tau_{30}$, and the x-ray structure. Interestingly, the constriction zone is maintained by a stretch of residues from Leu-17 to Val-21 regardless of the channel expansion as $\delta\tau$ increases; previous mutagenesis studies on the corresponding residues in Eco-MscL illustrate the importance of these residues in the tension-dependent gating process (44). A_{pore} in the periplasmic region (Thr-35 to Ile-38) increases from 65 Å^2 in the x-ray structure to 539 ± 57 Å^2 at $\delta\tau = 30°$. In contrast, the A_{pore} change at the constriction zone is moderate, only increased by 42 ± 12 Å^2. Although it is small, the constriction zone is large enough to create a water pathway in
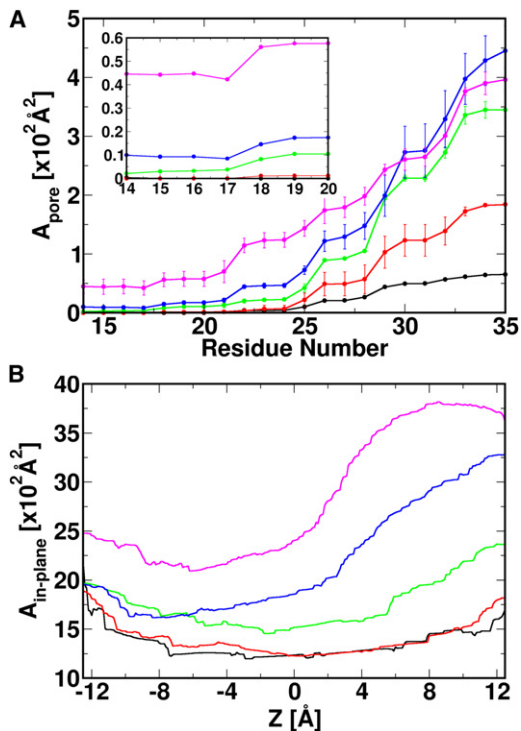
FIGURE 3 (*A*) Solvent accessible area profile along TM1 residues. The inset shows A$_{pore}$ near the constriction zone. The SDs are calculated from 5-ns sequential trajectory pieces in the last 30-ns simulation. (*B*) A$_{in-plane}$ profile along the *Z* axis. Area profiles are plotted for the x-ray structure (*black*), $\delta\tau_1$ (*red*), $\delta\tau_{10}$ (*green*), $\delta\tau_{20}$ (*blue*), and $\delta\tau_{30}$ (*magenta*).

FIGURE 4 (*A*) Definitions of the TM azimuthal angle (β). The structure of Tb-MscL at $\delta\tau = 30°$ is shown in tubular cartoon presentation with highlighted subunit A (*red*) and its pivot region from Leu-17 to Val-21 (*blue*). *a* is the helix axis. O is the center of mass of the channel. (*B*) Average azimuthal angle (β) and its SD of TM1 (*top*) and TM2 (*bottom*) in Tb-MscL subunits (*red*, *green*, *blue*, *magenta*, and *cyan*) as a function of $\delta\tau$.

Tb-MscL; 42 Å^2 corresponds to the cross-sectional area of seven water molecules and an effective radius of 3.7 Å. At the largest $\delta\tau$ (30°), the inward (from the periplasmic side to the cytoplasmic side), and outward water crossing rates, calculated by counting the water molecules crossing the *XY* plane in the constriction zone, are 2113 ns^{-1} and 2104 ns^{-1}. However, due to the stochastic nature and current simulation time, no ion permeation is observed.

Fig. 3 *B* shows the in-plane (cross-sectional) protein area (A$_{in-plane}$) along the *Z* axis. During TM helix tilting, the largest expansion occurs at the periplasmic side: from 1073 Å^2 (x-ray) to 3603 $\pm$ 6 Å^2 ($\delta\tau_{30}$). A$_{in-plane}$ of the expanded Tb-MscL at $\delta\tau = 30°$ corresponds to a channel with an outer diameter of ~68 Å, almost equivalent to that of the suggested fully opened channel (15). The A$_{in-plane}$ change, ΔA$_{in-plane}$, at the cytoplasmic side is much smaller, only 295 $\pm$ 24 Å^2. An average ΔA$_{in-plane}$, calculated using both ΔA$_{in-plane}$ at the cytoplasmic ($Z = -12.5$ Å) and periplasmic ($Z = 12.5$ Å) sides, is 1413 Å^2, well within the expanded area (580 to 2080 Å^2) estimated from individual membrane patches in the patch clamp experiments (10). These observations, together with the finding that Tb-MscL with large $\delta\tau$ conducts water, support that TM helix tilting in the current study results in an expanded Tb-MscL structure, i.e., an intermediate structure between the closed and the fully open Tb-MscL.
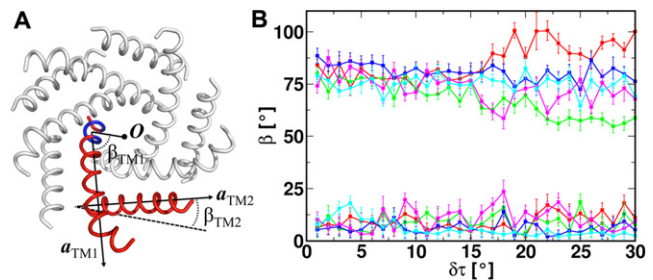
We examine the change in TM helix orientation as Tb-MscL expands in terms of TM azimuthal angle (β); β is defined as the angle between the *XY* plane projections of a TM helix principal axis and a reference vector from the center of mass of the constriction-zone residues (Leu-17 to Val-21) to the center of mass of the channel (Fig. 4 *A*). The basis of choosing such a reference vector is that the center of mass positions of both the constriction zone and the channel are almost invariant. Because the helix tilt restraint force is only exerted on the Cα atoms that define the helical axis, TM helices can change their spatial arrangement, depending on TM-TM and TM-environment interactions, whereas their tilt angle is maintained at the target value. Therefore, the evolution of TM orientation in terms of β along $\delta\tau$ could be a good measure of Tb-MscL expansion pathway. As shown in Fig. 4 *B*, although β_{TM1} of subunit A shows an increase of 16 $\pm$ 4° from $\delta\tau = 1°$ to 30°, it decreases by 21 $\pm$ 4°, 12 $\pm$ 6°, 6 $\pm$ 7°, and 10 $\pm$ 4° for the B, C, D, and E subunits, respectively. By definition, the decrease in β_{TM1} indicates that there is a right-handed twisting motion of TM1 occurring simultaneously with the constriction zone expansion. More specifically, TM1 tilting makes its periplasmic end swing toward the pore axis and moves its cytoplasmic end away from the pore axis, resulting in an iris-like opening, similar to what was proposed in the gating model of Tb-MscL and Eco-MscL (45); the exception in subunit A is discussed below in the context of TM rearrangement for the transition from an expanded to a fully open state. Unlike β_{TM1}, there is no significant difference in β_{TM2}, either between the systems with different $\delta\tau$ or between the individual subunits, indicating that the motion of TM2 is different from that of TM1; instead of tilting and twisting, TM2 helices tilt and move outward, away from the pore axis.

Free energy change upon TM helix tilting

Fig. 2 *C* shows the total PMF, i.e., the sum of the PMFs from all TM helices, as a function of $\delta\tau$ from the last 30-ns

trajectory of each system. We examine the PMF convergence by dividing the last 30-ns trajectory into 5-ns sequential pieces and calculating the SD from the 5-ns PMFs. The largest fluctuation of the total PMF is 8.7 kcal/mol at $\delta\tau = 30°$ and the SD of each TM helix PMF is small, mostly below 2.0 kcal/mol, supporting the overall convergence of the PMF profiles.

The free energy change (ΔG_{MscL}) from the Tb-MscL x-ray structure is correlated with the work done by γ_{ex} (i.e., $\Delta G_{TENSION} = \gamma_{ex} \times \Delta A_{in\text{-}plane}$). The correspondence between ΔG_{MscL} and $\Delta G_{TENSION}$ is not incidental; they are of similar magnitude and both increase as a function of $\delta\tau$ (Fig. 2 C). This indicates that TM tilting would result in an expanded channel that can also be achieved by applying a surface tension, echoing the proposed TM tilting mechanism for the MscL opening (15). ΔG_{MscL} (18.1 ± 3.4 kcal/mol at $\delta\tau = 16°$ and 57.9 ± 8.7 kcal/mol at $\delta\tau = 30°$) is also comparable of that (8.2–31.3 kcal/mol) measured using Eco-MscL in giant spheroplasts (10), although direct comparison between the two free energies is not possible due to the aforementioned complications arising from the use of Tb-MscL and DMPC bilayer in the simulations. Nonetheless, examining the contributions from different components to the total free energy is still valid and provides valuable insights into the causes of MscL conformational change upon expansion.

Fig. S4 shows the contribution from each TM1 (ΔG_{TM1}) and TM2 (ΔG_{TM2}) to the total PMF as a function of $\delta\tau$, and the values at $\delta\tau = 30°$ are summarized in Table S2. In total, all TM2 supply 44.1 kcal/mol to ΔG_{MscL} upon channel expansion/opening, whereas the contribution from TM1 is only 13.8 kcal/mol. Such a difference asserts that the major contribution to ΔG_{MscL} arises from the expansion of TM2. Unlike the TM2 expansion, TM1 conformational change (tilting and twisting) does not require much energy input. As a result, once Tb-MscL reaches an expanded state with outer dimensions similar to a fully open channel, TM1 may rearrange and facilitate the transition to a fully open channel.

Using the mean force integration technique based on Eq. 1, the PMF of each TM can be further decomposed into the contributions from TM-TM ($\Delta G_{TM\text{-}TM}$), TM-membrane ($\Delta G_{TM\text{-}MEMB}$), and TM-solvent ($\Delta G_{TM\text{-}SOLV}$) interactions. The decomposition result is shown in Fig. S5, and Table S3 summarizes the change in each component between the closed (the x-ray structure) and the observed expanded channel ($\delta\tau_{30}$). In general, $\Delta G_{TM\text{-}MEMB}$ is small and similar in both TM1 and TM2. For TM1, this is because they form the channel lumen and do not interact directly with the membrane. In the case of TM2, while in contact with the DMPC bilayer, they do maintain hydrophobic match with the surrounding bilayer as they tilt (Fig. 2 B), which keeps $\Delta G_{TM\text{-}MEMB}$ small. In contrast to $\Delta G_{TM\text{-}MEMB}$, TM1 have much larger $\Delta G_{TM\text{-}SOLV}$ than TM2. There is also a weak negative correlation between $\Delta G_{TM\text{-}SOLV}$ and

$\Delta G_{TM\text{-}TM}$ in TM1; an increase in $\Delta G_{TM\text{-}SOLV}$ is mostly accompanied by a decrease in $\Delta G_{TM\text{-}TM}$ or vice versa (Fig. S5). It is such a balance that results in the relatively small ΔG_{TM1}, which may also be the case during further TM1 rearrangement.

Unlike TM1, $\Delta G_{TM\text{-}TM}$ is the predominant contribution to ΔG_{TM2}. In the closed Tb-MscL structure (6), TM2 interacts with TM1 from both the same and the neighboring subunits. As shown by a small change in the intersubunit TM1-TM2 distance ($D_{TM1\text{-}TM2}$), from 10.2 ± 0.1 Å (x-ray structure) to 11.2 ± 0.6 Å ($\delta\tau = 30°$) (Fig. 5), the contact interface between TM1 and the TM2 of the adjacent subunit is well preserved during TM helix tilting; the interfacial residues, namely Val-19, Ile-23, Ala-26, Leu-30, and Phe-34 on TM1 and Leu-72, Ala-75, Phe-79, Ile-82, and Val-86 on TM2, are unchanged as illustrated in Fig. 6, A and B. The analogous interaction pattern is also observed in the crystal structure of expanded Sa-MscL (Fig. 6 C) (8), with residues corresponding to those in the interfaces in Tb-MscL. This implies the important role of these residues in intersubunit TM interactions. The similarity observed between the TM interfaces also corroborates the biological relevance of the expanded Tb-MscL structures that resulted from the current study. On the other hand, the channel expansion process largely disrupts the interaction network between TM1 and TM2 in the same subunit; the intrasubunit $D_{TM1\text{-}TM2}$ increases from 14.4 ± 0.1 Å (x-ray structure) to 20.4 ± 1.7 Å ($\delta\tau = 30°$) (Fig. 5). This increase in the intrasubunit $D_{TM1\text{-}TM2}$ determines the large contribution of $\Delta G_{TM\text{-}TM}$ to ΔG_{TM2}. The changes in the interaction network include the breakage of an H-bond between the hydroxyl group in Thr-35 and the amide group in Asn-78 and the loss of hydrophobic interaction between Val-31 and Leu-81 (see Fig. S6, A and B).

How does an expanded structure proceed to a fully open one? Unfortunately, the time scale of such an event is beyond the current simulations. However, the aforementioned energetic consideration, e.g., a balance between
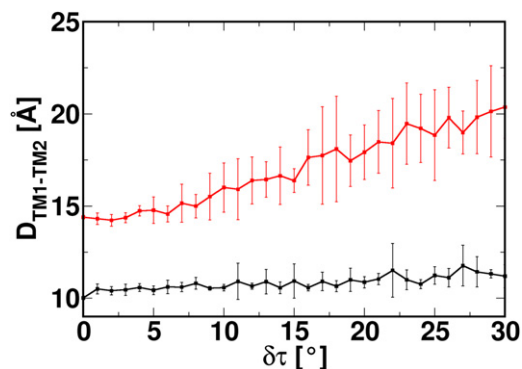

FIGURE 5   Average pairwise Cα-Cα distance between TM1 (Val-15-Thr-35) and TM2 (Leu-89-Leu-69) from the same subunit (*red*) and the neighboring subunit (*black*) at each $\delta\tau$.
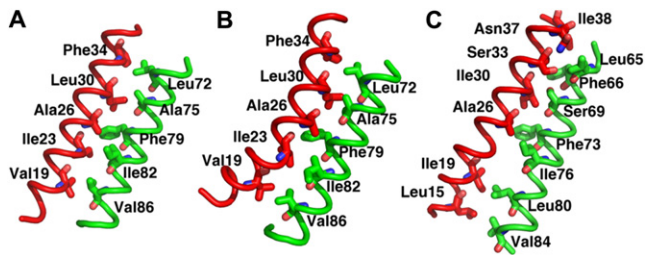
FIGURE 6 Interfacial residues between TM1 (*red*) and TM2 (*green*) in adjacent subunits: (*A*) Tb-MscL system $\delta\tau_1$, (*B*) Tb-MscL system $\delta\tau_{30}$, and (*C*) Sa-MscL x-ray structure. The helices are shown in tube representation with the interfacial residues highlighted by sticks.

$\Delta G_{\text{TM-SOLV}}$ and $\Delta G_{\text{TM-TM}}$ in ΔG_{TM1}, suggests that such transition involving TM1 rearrangement does not require significant energy input. This argument is also supported by the fact that the most work from the applied tension ($\Delta G_{\text{TENSION}}$) is used to expand the MscL channel (ΔG_{MscL}), as shown in Fig. 2 *C*. We speculate that the TM1 rearrangement is likely to be initiated by the increased mobility of TM1 after $\delta\tau = 15°$ as illustrated by heterogeneous β changes in different subunits (Fig. 4 *B*); such increase is also observed in the electron paramagnetic resonance experiments of an Eco-MscL trapped in an open state (15). When $\delta\tau$ is small, β_{TM1} in all subunits are similar to each other and invariant, implying a symmetric expansion of the wall formed by TM1 (Fig. 7, *A* and *B*). This symmetric expansion is limited by the optimal hydrophobic packing between the cytoplasmic end residues (including the constriction zone), preventing the channel from further opening (Fig. 7 *B*). As TM tilt more, TM1 in different subunits may have different β_{TM1} because of different intrasubunit and intersubunit TM1 and TM2 interactions governing β_{TM1}. With decreased β_{TM1} (all subunits except the subunit A in Fig. 4 *B*), the cytoplasmic ends of the TM1 move away from each other,

reducing the favorable intersubunit hydrophobic interactions in the constriction zones. However, the extent of such motions is limited because TM2 stop expanding after the channel reaches the outer dimension of the fully open state. To completely disrupt the hydrophobic interactions in the constriction zone and fully open the channel, an asymmetric motion of TM1 is needed. In the current simulations, this asymmetric motion is provided by the increase in β_{TM1} in subunit A (Fig. 7 *C*), which results in the disruption of the hydrophobic interactions between residues in the constriction zone, and may lead to the complete opening of the channel. It is also possible that increase in TM1 mobility is accompanied by change in its τ, i.e., TM1's τ changes after TM2 finishes expanding to complete the full close-to-open transition. However, the magnitude of this change might be small, because the open pore is lined primarily by the TM1 helices (15) and a tilt angle of ~70° for TM1 is expected (46) to produce a pore radius that is compatible with an open channel.

CONCLUDING DISCUSSION

We conclude our free energy MD simulation study by discussing possible Tb-MscL gating mechanisms in terms of membrane tension, lipid adaptation, conformational changes, and energetics. Fig. 2 *A* shows that tilting the Tb-MscL TM helices ($\delta\tau$, simulation) results in equivalent system expansion as applying an excess surface tension (γ_{ex}, experiment), and these two are linearly related. This supports the underlying hypothesis that the initial major response of Tb-MscL to increased membrane tension γ_{ex}, possibly from osmotic stress, is the expansion of Tb-MscL via TM helix tilting (Fig. S1, Figs. 2 *A* and 3). The hypothesis is further corroborated by the correspondence between the free energy increase of Tb-MscL as a function of $\delta\tau$ and the work done by γ_{ex} (Fig. 2 *C*).
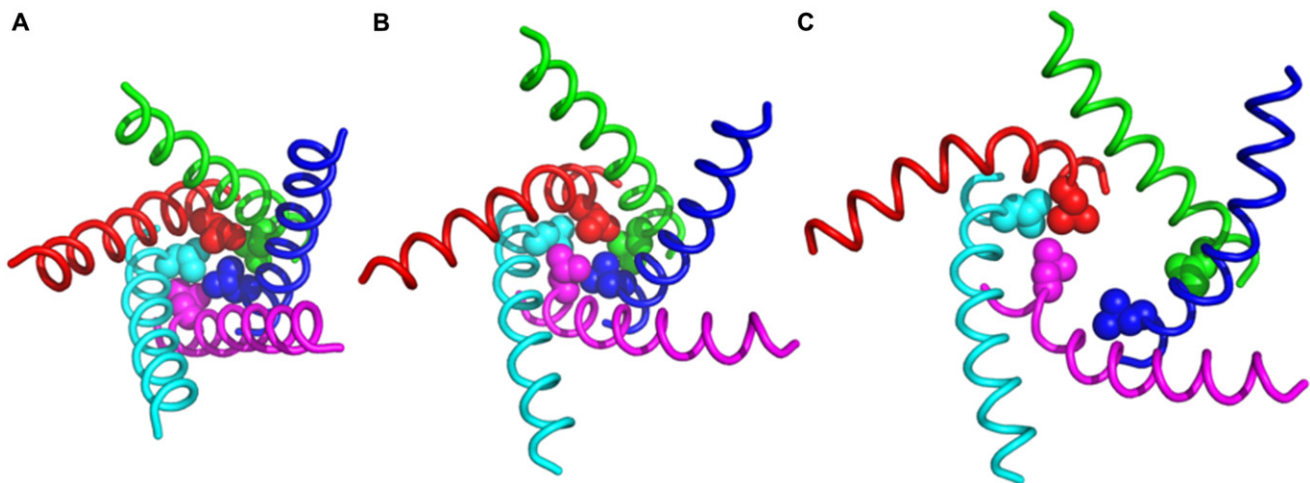

FIGURE 7 Molecular representation of TM1 in all subunits (*red*, *green*, *blue*, *magenta*, and *cyan*) in system (*A*) $\delta\tau_1$, (*B*) $\delta\tau_{15}$, and (*C*) $\delta\tau_{30}$. The side chain heavy atoms of constriction zone residue Leu-17 are highlighted in sphere representation.

Upon TM helix tilting, thinning of lipid bilayer occurs (*black line* in Fig. 2 *B*), as one would expect for a system with an applied tension. However, if the thinning effect is the result of an applied tension, its small magnitude seems insufficient to drive the TM helix tilting. Although such an observation is counterintuitive to a general MscL gating mechanism that one might envision, it is possible under the following two scenarios. First, TM helix tilting rather than membrane thinning is the direct response to γ_{ex}. This scenario requires that the elastic modulus of Tb-MscL during the initial expansion is smaller than that of the bilayer membrane. Such requirement could be satisfied, given the fact that there is an overlap between the measured elastic moduli for proteins ($1.8–20.4 \times 10^{10}$ dyn/cm^2) (47) and dipalmitoylphosphatidylcholine bilayers ($1.3–1.9 \times 10^{10}$ dyn/cm^2) (39). Second, the effect of γ_{ex} is mostly shown as the thinning of the local lipid bilayer, which is in direct contact with the MscL channel. The prerequisite for this hypothesis lies in that lipid-protein interactions are weaker than those between lipid molecules themselves. When tension is applied, the local bilayer is more sensitive; it loses part of its interactions with the channel and becomes thinner while the rest of the bilayer experiences less thinning effects. The large local thinning effect (Fig. 2 *B*) leads to TM tilting and ultimately the channel opening. This scenario finds its supports from the experimental observations that MscL opening is modulated by lipids that are in immediate vicinity to the protein (48) and the gating tension threshold is higher in bilayers containing phosphatidylethanolamine than pure phosphatidylcholine bilayers (9). Phosphatidylethanolamine could strengthen the interactions between protein and local lipid by i), forming an H-bond network with MscL and ii), having a larger hydrophobic thickness than phosphatidylcholine with the same lipid tails (49,50). Nonetheless, extra experimental and computational work systematically investigating impacts from both lipid tail length and lipid headgroup is needed to test these hypotheses.

During the course of TM tilting, channel expansion is observed. At $\delta\tau = 16°$, the pore radius of the constriction zone reaches to 2.4 Å, and the pore becomes water permeable. The expanded structure represents an intermediate between the closed and the fully open states. The free energy required to achieve this expanded state is similar in magnitude to the work done by the applied tension γ_{ex} (Fig. 2 *C*). In addition, energy decomposition points out that the expanded Tb-MscL is the result of tilting and expansion of TM2, which facilitates TM1 tilting with iris-like motion (Fig. 4 *B*) via hydrophobic interactions between intersubunit TM1 and TM2 (Fig. 5). At the same time, the hydrophobic interactions between constriction zone residues on different subunits are weakened, giving TM1 more freedom, so that they can rearrange to form a fully open channel. The small contribution of TM1 to the total PMF, resulting from a balance between $\Delta G_{TM-SOLV}$ and

ΔG_{TM-TM} (Fig. S5 and Table S3), implies that the transition between the expanded and fully open Tb-MscL mainly lies in the rearrangement of the TM1 helices and does not involve extra work by the tension.

SUPPORTING MATERIAL

REFERENCES

1. Gillespie, P. G., and R. G. Walker. 2001. Molecular basis of mechanosensory transduction. *Nature.* 413:194–202.

2. Sukharev, S., and D. P. Corey. 2004. Mechanosensitive channels: multiplicity of families and gating paradigms. *Sci. STKE.* 2004:re4.

3. Betanzos, M., C. S. Chiang, …, S. Sukharev. 2002. A large iris-like expansion of a mechanosensitive channel protein induced by membrane tension. *Nat. Struct. Biol.* 9:704–710.

4. Sukharev, S. I., B. Martinac, …, C. Kung. 1993. Two types of mechanosensitive channels in the *Escherichia coli* cell envelope: solubilization and functional reconstitution. *Biophys. J.* 65:177–183.

5. Sukharev, S. I., P. Blount, …, C. Kung. 1994. A large-conductance mechanosensitive channel in *E. coli* encoded by mscL alone. *Nature.* 368:265–268.

6. Steinbacher, S., R. Bass, …, D. C. Rees. 2007. Structures of the prokaryotic mechanosensitive channels MscL and MscS. *Curr. Top. Membr.* 58:1–24.

7. Sukharev, S. I., W. J. Sigurdson, …, F. Sachs. 1999. Energetic and spatial parameters for gating of the bacterial large conductance mechanosensitive channel, MscL. *J. Gen. Physiol.* 113:525–540.

8. Liu, Z., C. S. Gandhi, and D. C. Rees. 2009. Structure of a tetrameric MscL in an expanded intermediate state. *Nature.* 461:120–124.

9. Moe, P., and P. Blount. 2005. Assessment of potential stimuli for mechano-dependent gating of MscL: effects of pressure, tension, and lipid headgroups. *Biochemistry.* 44:12239–12244.

10. Chiang, C. S., A. Anishkin, and S. Sukharev. 2004. Gating of the large mechanosensitive channel in situ: estimation of the spatial scale of the transition from channel population responses. *Biophys. J.* 86:2846–2861.

11. Meyer, G. R., J. Gullingsrud, …, B. Martinac. 2006. Molecular dynamics study of MscL interactions with a curved lipid bilayer. *Biophys. J.* 91:1630–1637.

12. Gullingsrud, J., and K. Schulten. 2003. Gating of MscL studied by steered molecular dynamics. *Biophys. J.* 85:2087–2099.

13. Tang, Y., J. Yoo, …, X. Chen. 2008. Gating mechanisms of mechanosensitive channels of large conductance, II: systematic study of conformational transitions. *Biophys. J.* 95:581–596.

14. Wiggins, P., and R. Phillips. 2004. Analytic models for mechanotransduction: gating a mechanosensitive channel. *Proc. Natl. Acad. Sci. USA.* 101:4071–4076.

15. Perozo, E., D. M. Cortes, …, B. Martinac. 2002. Open channel structure of MscL and the gating mechanism of mechanosensitive channels. *Nature.* 418:942–948.

16. Lee, J., and W. Im. 2007. Restraint potential and free energy decomposition formalism for helical tilting. *Chem. Phys. Lett.* 441:132–135.

17. Jo, S., J. B. Lim, …, W. Im. 2009. CHARMM-GUI Membrane Builder for mixed bilayers and its application to yeast membranes. *Biophys. J.* 97:50–58.

18. Jo, S., T. Kim, and W. Im. 2007. Automated builder and database of protein/membrane complexes for molecular dynamics simulations. *PLoS ONE.* 2:e880.

19. Jo, S., T. Kim, …, W. Im. 2008. CHARNIM-GUI: a web-based graphical user interface for CHARMM. *J. Comput. Chem.* 29:1859–1865.

20. Anishkin, A., V. Gendel, …, S. Sukharev. 2003. On the conformation of the COOH-terminal domain of the large mechanosensitive channel MscL. *J. Gen. Physiol.* 121:227–244.

21. Blount, P., S. I. Sukharev, …, C. Kung. 1996. Single residue substitutions that change the gating properties of a mechanosensitive channel in *Escherichia coli. Proc. Natl. Acad. Sci. USA.* 93:11652–11657.

22. Feller, S. E., Y. H. Zhang, …, B. R. Brooks. 1995. Constant-pressure molecular-dynamics simulation - the langevin piston method. *J. Chem. Phys.* 103:4613–4621.

23. Klauda, J. B., N. Kucerka, …, J. F. Nagle. 2006. Simulation-based methods for interpreting x-ray data from lipid bilayers. *Biophys. J.* 90:2796–2807.

24. Skibinsky, A., R. M. Venable, and R. W. Pastor. 2005. A molecular dynamics study of the response of lipid bilayers and monolayers to trehalose. *Biophys. J.* 89:4111–4121.

25. Rui, H. A., and W. Im. 2010. Protegrin-1 orientation and physicochemical properties in membrane bilayers studied by potential of mean force calculations. *J. Comput. Chem.* 31:2859–2867.

26. Klauda, J. B., R. M. Venable, …, R. W. Pastor. 2010. Update of the CHARMM all-atom additive force field for lipids: validation on six lipid types. *J. Phys. Chem. B.* 114:7830–7843.

27. Dolan, E. A., R. M. Venable, …, B. R. Brooks. 2002. Simulations of membranes and other interfacial systems using P2(1) and Pc periodic boundary conditions. *Biophys. J.* 82:2317–2325.

28. Brooks, B. R., C. L. Brooks, III, …, M. Karplus. 2009. CHARMM: the biomolecular simulation program. *J. Comput. Chem.* 30:1545–1614.

29. MacKerell, A. D., D. Bashford, …, M. Karplus. 1998. All-atom empirical potential for molecular modeling and dynamics studies of proteins. *J. Phys. Chem. B.* 102:3586–3616.

30. MacKerell, Jr., A. D., M. Feig, and C. L. Brooks, 3rd. 2004. Extending the treatment of backbone energetics in protein force fields: limitations of gas-phase quantum mechanics in reproducing protein conformational distributions in molecular dynamics simulations. *J. Comput. Chem.* 25:1400–1415.

31. Jorgensen, W. L., J. Chandrasekhar, …, M. L. Klein. 1983. Comparison of simple potential functions for simulating liquid water. *J. Chem. Phys.* 79:926–935.

32. Steinbach, P. J., and B. R. Brooks. 1994. New spherical-cutoff methods for long-range forces in macromolecular simulation. *J. Comput. Chem.* 15:667–683.

33. Essmann, U., L. Perera, …, L. G. Pedersen. 1995. A smooth particle mesh Ewald potential. *J. Chem. Phys.* 103:8577–8592.

34. Chang, G., R. H. Spencer, …, D. C. Rees. 1998. Structure of the MscL homolog from *Mycobacterium tuberculosis*: a gated mechanosensitive ion channel. *Science.* 282:2220–2226.

35. Allen, T. W., O. S. Andersen, and B. Roux. 2004. Energetics of ion conduction through the gramicidin channel. *Proc. Natl. Acad. Sci. USA.* 101:117–122.

36. Lee, J., and W. Im. 2008. Role of hydrogen bonding and helix-lipid interactions in transmembrane helix association. *J. Am. Chem. Soc.* 130:6456–6462.

37. Im, W., J. Lee, …, H. Rui. 2009. Novel free energy calculations to explore mechanisms and energetics of membrane protein structure and function. *J. Comput. Chem.* 30:1622–1633.

38. Kumar, S., D. Bouzida, …, J. M. Rosenberg. 1992. The weighted histogram analysis method for free-energy calculations on biomolecules. 1. The method. *J. Comput. Chem.* 13:1011–1021.

39. Venable, R. M., A. Skibinsky, and R. W. Pastor. 2006. Constant surface tension molecular dynamics simulations of lipid bilayers with trehalose. *Mol. Simul.* 32:849–855.

40. Evans, E., and W. Rawicz. 1990. Entropy-driven tension and bending elasticity in condensed-fluid membranes. *Phys. Rev. Lett.* 64: 2094–2097.

41. Moe, P. C., G. Levin, and P. Blount. 2000. Correlating a protein structure with function of a bacterial mechanosensitive channel. *J. Biol. Chem.* 275:31121–31127.

42. Perozo, E., A. Kloda, …, B. Martinac. 2002. Physical principles underlying the transduction of bilayer deformation forces during mechanosensitive channel gating. *Nat. Struct. Biol.* 9:696–703.

43. Ursell, T., K. C. Huang, …, R. Phillips. 2007. Cooperative gating and spatial organization of membrane proteins through elastic interactions. *PLOS Comput. Biol.* 3:803–812.

44. Yoshimura, K., A. Batiza, …, C. Kung. 1999. Hydrophilicity of a single residue within MscL correlates with increased channel mechanosensitivity. *Biophys. J.* 77:1960–1972.

45. Sukharev, S., M. Betanzos, …, H. R. Guy. 2001. The gating mechanism of the large mechanosensitive channel MscL. *Nature.* 409:720–724.

46. Strop, P., R. Bass, and D. C. Rees. 2003. Prokaryotic mechanosensitive channels. *Adv. Protein Chem.* 63:177–209.

47. Mori, K., Y. Seki, …, K. Soda. 2006. Evaluation of intrinsic compressibility of proteins by molecular dynamics simulation. *J. Chem. Phys.* 125:054903.

48. Powl, A. M., J. M. East, and A. G. Lee. 2008. Importance of direct interactions with lipids for the function of the mechanosensitive channel MscL. *Biochemistry.* 47:12175–12184.

49. Kucerka, N., Y. Liu, …, J. F. Nagle. 2005. Structure of fully hydrated fluid phase DMPC and DLPC lipid bilayers using X-ray scattering from oriented multilamellar arrays and from unilamellar vesicles. *Biophys. J.* 88:2626–2637.

50. Nagle, J. F., and S. Tristram-Nagle. 2000. Structure of lipid bilayers. *Biochim. Biophys. Acta.* 1469:159–195.

51. DeLano, W. L. 2002. The PyMOL Molecular Graphics System. DeLano Scientific, Palo Alto, CA.